Thermodynamic Analysis of Nickel (II) and Zinc (II) Adsorption to Biochar

Md. Samrat Alam,[1] Drew Gorman-Lewis,[2] Ning Chen,[3] Shannon L. Flynn,[1,4] Yong Sik Ok[5], Kurt O. Konhauser,[1] Daniel S. Alessi[1*]

[1]Department of Earth & Atmospheric Sciences, 1-26 Earth Sciences Building, University of Alberta, Alberta, T6G 2E3, Canada
[2]Department of Earth and Space Sciences, University of Washington, Johnson Hall Rm-070, Box 351310, 4000 15th Avenue, NE Seattle, WA 98195, USA
[3]Canadian Light Source Inc., University of Saskatchewan, 114 Science Plane, Saskatoon, SK, S7N 0X4, Canada
[4]School of Natural and Environmental Sciences, Newcastle University, Newcastle upon Tyne, NE1 7RU, United Kingdom
[5]Korea Biochar Research Center, OJeong Eco-Resilience Institute & Division of Environmental Science and Ecological Engineering, Korea University, Seoul 02841, Korea

ABSTRACT

While numerous studies have investigated metal uptake from solution by biochar, few of these have developed a mechanistic understanding of the adsorption reactions that occur at the biochar surface. In this study, we explore a combined modeling and spectroscopic approaches for the first time to describe the molecular level adsorption of Ni(II) and Zn(II) to biochar using five types of biochar. Following thorough characterization, potentiometric titrations were carried out to measure the proton (H^+) reactivity of each biochar, and the data was used to develop protonation models. Surface complexation modeling (SCM) supported by synchrotron-based extended X-ray absorption fine structure (EXAFS) was then used to gain insights into the molecular scale metal-biochar surface reactions. The SCM approach was combined with isothermal titration calorimetry (ITC) data to determine the thermodynamic driving forces of metal adsorption. Our results show that the reactivity of biochar towards Ni(II) and Zn(II) directly relates to the site densities of biochar. EXAFS along with FT-IR analyses, suggest that Ni(II) and Zn(II) adsorption occurred primarily through proton-active carboxyl (–COOH) and hydroxyl (–OH) functional groups on the biochar surface. SCM-ITC analyses revealed that the enthalpies of protonation are exothermic and Ni(II) and Zn(II) complexes with biochar surface are slightly exothermic to slightly endothermic. The results obtained from these combined approaches contribute to the better understanding of molecular scale metal adsorption onto the biochar surface, and will facilitate the further development of thermodynamics-based, predictive approaches to biochar removal of metals from contaminated water.

1. INTRODUCTION

Biochar is a carbon-rich solid produced through the carbonization and/or pyrolysis of biomass derived from a variety of feedstocks, including straw, wood, and organic industrial wastes.[1-3] It has proven effective in the removal of organic and metal contaminants from water,[4-8] is considered a prospective alternative to activated carbon (AC) for water treatment and soil amendment purposes due to its lower production cost, and it is also thought to act as a global "carbon-sink".[8-10] The efficiency of contaminant removal from water by biochar depends on several factors, including contaminant concentration and the distribution and types of surface functional groups, the latter of which can vary widely depending on the pyrolysis temperature and types of feedstock used during production.[11-13] Relatively modest concentrations of Ni and Zn in water (> 10 µg/L for Ni and > 5mg/L for Zn) are shown to have toxic effects on human health. Geogenic and anthropogenic inputs, especially from tanneries, smelters, or sewage sludge application, can increase Ni and Zn concentrations in the environment.[14-15] Therefore, understanding the mechanisms by which environmentally relevant divalent metals such as Ni and Zn are removed from aqueous solution by biochar is critical to assessing its use as an adsorbent.

Key to developing rigorous geochemical models that can accurately predict the removal of metal cations from solution by biochar is the identification and quantification of surface functional groups (sites), their protonation constants, and the reactivity towards specific metals.[16-27] Metal adsorption data can be modeled using two general categories of models: (i) empirical models such as isotherms such as Freundlich and Langmuir, and (ii) thermodynamic approaches such as surface complexation modeling (SCM). Empirical models normally cannot account for changes in metal concentration, pH, ionic strength, temperature and complexation or for the effect of competing ions for sorbent sites. For this reason, the application of empirical partitioning constants to predict metal distribution in dynamic environmental systems can be

problematic.[16-17] In contrast, the SCM approach has been proven to be an effective method to predict the acid/base and ion/metal binding behaviors of a variety of environmental surfaces, and in systems approaching the complexity of those found in nature.[16-26] The primary advantage of using a SCM approach over empirical approaches is that the distribution of metals in a system can be predicted using the stability constants determined experimentally for individual sorbent-metal surface complexes, because the surface complexation theory is grounded in balanced chemical reactions, and ultimately, in chemical thermodynamics.[16-17]

Recent studies which have modeled metal sorption by biochar have primarily relied on empirical metal adsorption models.[2-3,5-7,11,26] To our knowledge, few studies have applied a SCM approach to biochar: Zhang and Luo[28] modeled copper (Cu) adsorption to biochar; Vithanage et al.[29] modeled antimony (Sb) adsorption to biochar; and Alam et al.[30] modeled the adsorption of selenium (Se) and cadmium (Cd) to biochar-amended agricultural soils. While these studies proposed SCMs that successfully describe the adsorption of metal ions onto sorbents across variable chemical conditions, they do not provide direct measurements of the surface coordination of adsorbed ions.

Here we apply two thermodynamic approaches, (i) surface complexation modeling (SCM) and (ii) isothermal titration calorimetry (ITC), supported by synchrotron-based X-ray absorption spectroscopy (XAS) to develop a predictive and mechanistic model of metal binding to biochar. Synchrotron-based extended X-ray absorption fine structure (EXAFS) studies are a powerful tool to identify the atomic metal-surface coordination environment.[31-34] ITC measurements were further conducted to determine the thermodynamic driving force (e.g., bond formation, dehydration, enthalpy and entropy) of the metal-surface reaction(s). Understanding the thermodynamic driving forces of adsorption provides critical insights into the reasons why

spontaneous adsorption reactions occur, as well as the temperature dependence of these reactions.[35-39] In this study, we aim to: (1) determine whether the surface complexation modeling approach can accurately predict Ni(II) and Zn(II) adsorption (as model divalent cations) to five types of biochar, (2) explore the metal-biochar surface reactions at molecular level, and (3) determine the thermodynamic driving forces of metal-biochar surface reactions. Using a varied set of biochar allowed us to investigate the potential effects of production scale, differing sources of biomass, and pyrolysis temperature on the metal adsorption behavior. Our study is the first to develop a predictive model of metal adsorption to biochar underpinned by a mechanistic understanding of the adsorption processes at the surface of biochar. As such, our work opens the door to future studies that use the SCM approach as a flexible, predictive method to determine the removal of metals from water by biochar in variable water chemistries.

2. MATERIALS AND METHODS

2.1 Biochar Preparation

Biochar produced from wheat straw (WS) and wood pin chips (WPC) were obtained from the Alberta Biochar Initiative (ABI; Vegreville, Alberta, Canada). The raw feedstocks of WS and WPC were placed in a prototype 1.0, batch carbonizer (Alberta Innovates Technology Futures, AITF), and in an auger retort carbonizer (ABRI- Tech, 1 Tonne Retort system; ABI, Vegreville, Alberta), respectively, and pyrolized under limited oxygen conditions. The residence time in both cases was 30 min at 500°C to 550°C. The biochar yield was 30 to 33% on the basis of dry mass. Sewage sludge biochar (SSBC) was produced at the Korea Biochar Research Center, Kangwon National University, at a lab scale as described in Ahmad et al.[12] The raw feedstocks were ground to <1 mm, and then dried at 60°C for 3 days. A muffle furnace (MF 21GS, Jeio Tech, Seoul, Korea) was used to pyrolyze the feedstock as follows: temperature was increased at

a rate of 7°C/min under limited oxygen conditions, and the feedstocks were held for 3 hours at 300°C, 500°C and 700°C, respectively, followed by cooling to room temperature inside the furnace.[12] These biochar are hereafter referred to as SSBC 300°C, SSBC 500°C, and SSBC 700°C.

2.2 Biochar Characterization

The proximate analyses, X-ray powder diffraction (XRD), elemental analysis, Brunauer-Emmett-Teller (BET) surface area analysis, Barret-Joyner-Halender (BJH) pore volume and pore size distribution, surface morphological characterizations using Scanning Electron Microscopy (SEM) coupled with Energy Dispersive Spectroscopy (EDS) and Fourier transform infrared spectroscopy (FT-IR) analyses of WS, WPC, SSBC 300°C, SSBC 500°C, and SSBC 700°C were carried out as described in Alam et al.[4,30] A detailed explanation of the biochar characterization methods is given in the Supporting Information (SI) section.

2.3 Potentiometric Titrations

Potentiometric titrations were conducted to determine the concentrations and protonation constants (K_a) values of proton-active surface functional groups. For each titration, ~0.2 g of dry biochar was suspended in 50 mL of 0.01 M $NaNO_3$ electrolyte solution. The sample containers were then sealed with Parafilm and purged with N_2 gas for 30 min prior to each titration and throughout the titration process to maintain a CO_2-free solution. For the forward titrations (pH 3-11) a solution of 0.1 M NaOH was used, and for the reverse titrations (pH 11-3) a 0.1 M HCl solution was used. Detailed titration methods and corresponding data modeling methods are reported in the SI section.

2.4 Ni and Zn Adsorption Experiments

Batch adsorption experiments were carried out using aqueous solutions of Ni(II) and Zn(II). A 8.5 mM stock solution of Ni was prepared from $Ni(NO_3)_2.6H_2O$, and a 1.7 mM of Zn stock solution from $ZnCl_2$. In polypropylene test tubes, 10 g/l of biochar was suspended in 0.01M $NaNO_3$ electrolyte solution and a volume of Ni and Zn stock solution was added to achieve the target initial metal concentrations of 170 µM and 17 µM, for both Ni and Zn. The final volume of each experiment was approximately 10 mL. The pH of metal adsorption experiments ranged from approximately 2.0 to 6.5, and was achieved by adding small volumes of concentrated NaOH or HCl. This pH range was selected to avoid the precipitation of Ni and/or Zn-hydroxides and/or carbonates, which were observed in control experiments above pH 6.5 and were predicted in aqueous Ni and Zn speciation diagrams generated for our experimental conditions (Figure S1).

Following pH adjustment, test tubes were then placed on a rotary shaker for 36 h to allow the pH to stabilize and for the adsorption of Ni and/or Zn to biochar surface functional groups to achieve equilibrium. Kinetics experiments were carried out to ensure that equilibrium had been achieved in 36 h (Figure S2). The tubes were then centrifuged at 5000 g for 10 min and the resulting supernatant was filtered through 0.45 µm nylon membranes (Millex HP). The filtered supernatants were then diluted 1:1 with 4N HNO_3 before Ni and Zn were analyzed using inductively coupled plasma - mass spectroscopy (ICP-MS/MS; Agilent 8800). Control experiments showed that there was no adsorption of Ni(II) and Zn(II) onto the tubes used for the metal adsorption experiments. Aqueous Ni and Zn standards for ICP-MS/MS calibration were prepared from SPEX CertiPrep Ni and Zn ICP-MS standards and diluted with 0.01M $NaNO_3$ to match the experimental matrix. The difference between the initial Ni or Zn concentration in each experiment and the measured remaining Ni or Zn concentration in solution after equilibration

was considered to be the amount adsorbed. To test competitive sorption of Ni and Zn to the biochar surface, Ni and Zn were mixed to a total initial concentration of 170 µM (85 µM Ni + 85 µM Zn) and 17 µM (8.5 µM + 8.5 µM Zn). The stock solution, pH adjustment, centrifugation, filtration, and acidification sampling procedures were the same as those described above for the individual-metal experimental systems. The experimental details of the kinetics experiments and details of the SCM approach used to model metal adsorption data are provided in the SI section.

2.5 EXAFS Data Collection and Analysis

X-ray absorption spectroscopy (XAS) was used to study the coordination environments of Ni(II) and Zn(II) adsorbed to WS biochar, in experiments conducted at pH 6.5 at initial metal concentrations of 17 µM for single-metal systems, and at 170 µM for both single-metal and Zn+Ni systems. EXAFS analyses of Ni- and Zn-sorbed biochar were carried out at the Ni and Zn K-edges (8333 eV and 9659 eV, respectively) at the Canadian Light Source (CLS) 06ID-1 Hard X-ray Micro-Analysis (HXMA) beamline. A Si (220) double crystal monochromator was calibrated to the pre-edge feature of Ni and Zn at 8333 eV and 9659 eV, respectively, and detuned 40% the monochromator second crystal to reject higher harmonic intensities. Spectra for $Ni(OH)_2$, $Zn(OH)_2$, and Ni acetate were recorded in transmission mode. Spectra for the Zn acetate reference material and Ni- and Zn-sorbed biochar samples were recorded in fluorescence mode using a 32-element Ge solid state detector.

IFEFFIT and the graphical interface ATHENA were used for background subtraction and X-ray absorption near edge structure (XANES) linear combination fitting.[40] EXAFS data fitting R space curve fitting was carried out using WinXAS (version 2.3).[40] The phase shift and backscattering amplitude function were generated theoretically with the FEFF 7 code[41] from the crystal structure data of the crystal structure of Ni(II) (aq), NiO, β-$Ni(OH)_2$, ZnO, $Zn(OH)_2$. The

R-space between 0.8 and 4.2 Å was considered for the fits of Fourier transform (FT) k^3-weighted EXAFS data to FEFF models, and a k space data range used for the Fourier Transform is of 3 – 10 $Å^{-1}$. The amplitude reduction factor (S_0^2) was set to 1 for all fits. The shift in the threshold energy (E_0) was allowed to vary for R space fitting.[42-43]

2.6 Isothermal Titration Calorimetry (ITC)

The ITC experiments were carried out as described in Harrold and Gorman-Lewis[36] and Gorman-Lewis et al.[38] Briefly, a TAM III nanocalorimeter was used to measure the heat flux between a reference and reaction vessel as a function of time. The heat flow response by the calorimeter was calibrated by electrical heating, a procedure verified by measuring the heat of protonation of trishydroxymethylaminomethane (TRIS/THAM) at 25 °C.[44] Initially, both cells were filled with 10g/L biochar suspensions in 0.01M NaCl and placed in the calorimeter bath. Biochar suspensions for proton adsorption measurements were purged with N_2 for 30m prior to loading the suspensions into the reaction vessels, which were purged with N_2 and sealed. The reaction vessels were lowered into the calorimeter in 3 steps, pausing with each step to allow the calorimeter to equilibrate. After achieving thermal equilibration and a stable heat flow with the reaction cell stirred at 80 rpm, individual titrant doses were delivered into the reaction cell via cannula by a computer controlled syringe. The experimental details and modeling procedure for the ITC data are provided in the Supporting Information section.

3. RESULTS AND DISCUSSION

3.1 Characteristics of Biochar

The WS and WPC yield from the parent biomasses was approximately 30% (Table S1). The SSBC yield decreased from 70.1% to 50.3% as the temperature of pyrolysis increased from 300°C to 700°C, with the variation in yield in WS, WPC and SSBC due to differences in types of feedstock and production conditions. According to Keiluweit et al.[45] and Chen et al.[46], the

decomposition of lignin, cellulose, H_2O, CO_2, CO, CH_4 and H_2 from feedstock increases with increasing pyrolysis temperature, indicating mostly the loss of oxygen containing functional groups and contributing to the lower yield. The XRD pattern (Figure S3) of WS and WPC shows that quartz and calcite are the major detectable mineral phases. In SSBC, other minerals including albite, muscovite, kaolinite, microcline and pyrite are also detected as minor phases. WS and WPC are mainly composed of C, 70 wt% and 85 wt%, respectively, indicating higher carbonization (Table S2). However, SSBC has lower %C as compared to WS and WPC, and %C decreases with increasing pyrolysis temperature. The molar ratios of elements in each biochar were calculated to estimate their aromaticity (H/C) and polarity (O/C).[4,10] Both WS and WPC have relatively lower H/C and O/C molar ratios compared to the SSBC, except H/C at SSBC 700°C (Table S2), the difference was attributed to the different feedstocks. The molar H/C and O/C ratios in WS and WPC are likewise influenced by the relatively higher C content in their feedstocks as compared to SSBC. Higher pyrolysis temperatures generally lead to the removal of polar functional groups.[46-48] The surface area of WPC was markedly higher (224 m^2/g) than that of WS and SSBC (Table S2). In SSBC, a strong correlation between higher pyrolysis temperatures and higher surface area in the resulting biochar was observed (Table S2).

WS and WPC particles exhibit a flaky and rough surface (Figure S4A and S4B)[4], with a size range of 100 to 1000 μm, while SSBC particles (Figure S4C to S4E) are mostly angular and semi-spherical, and range in diameter between approximately 100 to 200 μm. There is no visible effect of pyrolysis temperature on the particle morphologies. Semi-quantitative elemental compositions estimated from EDS (Figure S5 and Table S3A and S3E) show that WS, WPC and SSBC are mainly composed of C and O, followed by Si, Al, Fe, P, K, Ca, Mg and S. The silica

nodules observed in WS and WPC likely contain silanol functional groups (>Si-OH) which would be proton-active and could complex metals.[4]

3.2 Potentiometric Titrations

All biochar types studied showed significant buffering capacity from pH 4 to 10 (Figure S6). Minimal variance was observed between forward and reverse titrations, suggesting reversibility of the protonation and deprotonation reactions on the biochar surface during the timescale of the experiments. Potentiometric titration data was modeled using a non-electrostatic, discrete site surface complexation model to determine the proton binding constants and site concentrations for the reactive surface sites for each biochar (Table 1). We defined three discrete site functional groups from lowest to highest pK_a (-log K_a) values for all five types of biochar. The three-site models were calculated using a least-squares optimization routine, as implemented in FITEQL 4.0.[49] In all cases the variance, or V(Y), values were in the range of $0.1<V(Y)<20$ (Table 1), which indicates a good fit to the titration data.[49] Modeling with three sites yielded a better fit than did modeling with one, two, or four sites.

The surface acidity of biochar is normally attributed to carboxyl groups (pK_a = 1.7−4.7), lactones or lactols (pKa = 6.37−10.25), and phenolic hydroxyl groups (pK_a = 9.5−13).[2-3,28,46-47,50-52] According to Achadu et al.[53], the hydrolysis of silicon dioxide during ashing produces silanol surface group (–SiOH) with a weak acidity (pK_a = 6-8). The modeling results show that the pK_a values for site 1 (pK_a 4.24 to 4.70) are similar for all five biochar types, and fall in the pK_a range for carboxyl groups. The proton-active site concentrations are highest for site 1 for all five biochar types, except SSBC at 700°C. pK_a values for site 2 and/or site 3 are variable across biochar types; however, they do correspond well to the pK_a values of lactones, phenolic hydroxyl and weak acidic silanol groups. With increasing temperature, the pK_a value of site 3 also

increases, which is consistent with previous studies by Ahmad et al.[12] and Chen et al.[46] that suggested a total acidity decrease with increasing pyrolysis temperature.

Due to the structural diversity of biochar, pK_a values vary widely, and it is, therefore, difficult to designate unequivocal chemical identities to each site based on pK_a values alone.[52] Therefore, employing FT-IR is crucial to identify the surface chemistry of biochar. In this regard, the C=O and C=C infrared stretching vibrations at 1700 and 1600 cm^{-1} intensify, indicating the presence of carboxyl C, and potentially the formation of lactones and esters (Figure S7A).[46-47,50-56] The prominent peaks at 1440 cm^{-1} and 1375 cm^{-1}, representing C=O stretching of ketones and O-H bending of phenols, respectively, are present in all five biochar types. The band at ~900 cm^{-1} could be attributed to Si-OH groups, due to the presence of Si nodules in biochar that identified by SEM-EDS and XRD analyses.[57] As the pyrolysis temperature increased for SSBC, the -OH stretching (3200-3600 cm^{-1}) attributed to water molecules loses intensity due to diminished hydration. Aliphatic and aromatic C-H stretching from 2850 to 3050 cm^{-1} also decreases as the pyrolysis temperature increases, which is supported by the proximate analyses. Both FT-IR analyses (Figure S7) and the pK_a values calculated from modeling potentiometric titration data (Table 1) suggest that -OH groups belong to both organic phenols and inorganic silanol groups.

3.3 Ni and Zn Adsorption onto Biochar

The adsorption of Ni and Zn increases with increasing pH from 2 to 6.5 for both 17 µM and 170 µM Ni and Zn concentrations for all five biochar types (Figure 1). Removal of both metals from aqueous solution is greatly influenced by biochar surface chemistry and surface area.[2-3] The Ni adsorption capacity of WPC is much higher than that of WS, an expected result as WPC has both higher surface area and site concentrations (Figure 1). SSBC 500°C showed the highest Ni adsorption amongst the three SSBC biochars, despite SSBC 700°C having a higher surface area

than SSBC 500°C. However, SSBC 500°C has a higher site concentration than either SSBC 300°C and SSBC 700°C, suggesting that Ni adsorption to SSBC is controlled by total site concentration. WPC (production temperature ~500°C) and SSBC 500°C have higher Ni adsorption capacities, even though SSBC 300°C and SSBC 700°C have higher site concentrations than WPC. In contrast, WPC has higher surface area compared to SSBC 300°C and SSBC 700°C, suggesting both physical and chemical adsorption played important roles in Ni adsorption.

Studies have shown the effectiveness of biochar and soil organic matter at removing Zn from aqueous solution than Ni, which is consistent with our adsorption experimental results (Figure 1).[58-60] Leaching studies (Table S4) showed that WPC and SSBC 300°C leached a maximum of 3 µM and 2 µM Zn, respectively, which is 10 to 20% of the 17 µM of Zn used in the lower concentration adsorption experiments. However, Zn leaching from WS, SSBC 500°C and SSBC 700 was negligible (few ppb). Because of the potential interference of Zn leaching on the observed removal of Zn from solution, we did not use WPC and SSBC 300°C for 17 µM Zn adsorption experiments. Zn leaching from WPC and SSBC at 300°C in 170 µM experiments only accounted for 1 to 2% of the total initial Zn concentration, and therefore, 170 µM was used for Zn adsorption experiments to these biochar types and subsequent surface complexation modeling. In the 17 µM experiments, SSBC 500°C and SSBC 700°C showed a higher adsorption capacity than WS. The higher site concentrations of SSBC 500°C and SSBC 700°C than for WS likely correspond to the higher degree of Zn adsorption. WPC also showed highest Zn adsorption capacity of all five biochar types, as was observed for Ni adsorption.

The adsorption capacity was further normalized by the surface area of the five biochar samples. This normalization procedure helped us to understand and compare the performances of

each biochar in removing Ni and Zn from solution, independent of the structure (i.e., the surface area and porosity of biochar). The results showed that SSBC 300°C has the highest metal adsorption densities while WPC has the lowest, for both Ni and Zn (Figure S8). The difference in metal adsorption densities of SSBC 300°C and WPC is consistent with the fact that SSBC 300°C and WPC also have the highest and lowest proton-active site densities, respectively (Table 1). Metal adsorption densities and reactive site densities decreased with increasing pyrolysis temperature for SSBC.[12] The molar H/C and O/C ratios also decreased with increasing pyrolysis temperature for SSBC (Table S2), and WS has higher reactive site densities and molar H/C and O/C ratios than does WPC (Table 1 and Table S2). Overall, the results suggest that the biochar properties are highly influenced by pyrolysis temperature, and the adsorption densities are directly dependent on the proton-active site densities and molar O/C ratios.

3.4 Ni(II) and Zn(II) coordination at the surface of biochar

Ni EXAFS analyses revealed that the Ni-O shell had a radial distance of 1.97 Å to 2.1 Å, with a coordination number of 6, indicating that Ni is in an octahedral environment (Figure 2; for a summary of fitting parameters see Tables S5 and S6). In contrast, the Zn-O distance of 1.97 Å indicates tetrahedral coordination. The first shell metal-oxygen distance could result from either hydration of the metal cations or the acidic functional groups of –OH and –COOH that adsorbed Ni and Zn at the biochar surfaces.[27-28] The parameters of the Ni-O and Zn-O first shell are similar to those of the aqueous Ni(II) and Zn(II) cations, suggesting that the primary hydration shell remains intact after sorption. The second Ni-O shell is best represented with 3.5 to 4 oxygen atoms ranging from 2.65 to 2.71 Å. There is no evidence of Ni-Ni and Zn-Zn in the second shell, excluding the possibilities of surface precipitation and polymerization.[30] The assignment of the Ni-C shell at approximately 3.3 Å and Zn-C at 2.08 Å to 2.16 Å indicates that Ni and Zn form

organo-metallic complexes with the surface of the biochar. This leads to the formation of inner-sphere surface complexes, and is consistent with acidic ligands (i.e., -COOH and -OH) coordinating with Ni and Zn.[31,34] The Ni-Si and Zn-Si distances at 3 to 3.3 Å indicate that Ni and Zn form inner-sphere complexes, and show that Ni and Zn can also bind to Si-OH groups.

To further investigate Ni and Zn coordination to the biochar surface, FT-IR spectra of biochar before and after Ni(II) and Zn(II) sorption were subsequently compared (Figure S7). After Ni(II) and Zn(II) sorption, there is a decrease in the infrared band at approximately 1700 cm^{-1} and 3200 cm^{-1}, which correspond to the C=O stretching mode of the free carboxyl group and –OH groups (Figure S7B).[51] These changes further support the coordination of carboxyl ions and phenolic hydroxyl groups with Ni(II) and Zn(II). Taken together, it can be concluded that the Ni(II) and Zn(II) are adsorbed to biochar primarily through coordination with both carboxyl and hydroxyl ligands at the surface of the biochar.

3.5 Surface complexation modeling

A non-electrostatic surface complexation modeling (NEM) approach was used to model the adsorption behavior of Ni and Zn onto each biochar, an approach previously confirmed to be effective in low ionic strength solutions (e.g., 0.01M $NaNO_3$).[61-63] It was assumed that proton, Ni and Zn adsorption were due to proton and metal cation interactions with discrete negatively charged organic acid functional groups on the biochar, similar to that demonstrated for various sorbents including, bacteria, clay, ferric hydroxides, and silica.[16-22] The NEM approach considers the protonation or deprotonation of each type of surface functional group and the equilibrium equation to quantify the metal adsorption reactions according to the following stoichiometries:

$$\mathrm{R-A}(H)^0 \leftrightarrow \mathrm{H^+ + R-A^-} \quad (1)$$

$$\mathrm{R-A^- + M^{++} \leftrightarrow R-A(M)^+} \quad (2)$$

where, R is the bulk biochar, and A represents the proton active functional groups to which a divalent metal M^{++} (that is, Ni^{++} or Zn^{++} in this study) can adsorb. We calculated the stability constants for Ni(II) and Zn(II) adsorption to biochar using the stoichiometry shown in reaction (2). The model also considered Ni(II) and Zn(II) aqueous hydrolysis reactions presented in Table S7. The model that invokes Ni and Zn adsorption to first two sites of the 3-site protonation model showed the best fit to the experimental data (Figure 1). A 3-site adsorption model that uses three pK_a values and corresponding site concentrations from the protonation model was unable to fit the experimental data, and a 1-site adsorption model poorly fit the experimental data (Figure S9 and Table S8). In 2-site adsorption models, the first two pK_a values and corresponding site concentrations from the 3-site protonation model were used.

In the 2-site adsorption models, the Zn adsorption stability constant ($K_{1,Zn}$) is marginally higher than that of Ni ($K_{1,Ni}$) in the 17 µM experiments for all types of biochar; however, WS, WPC and SSBC 300°C showed slightly lower K_1 values for Zn binding than for Ni in 170 µM experiments (Table 2). Numerous studies report that the stability of Zn complexed with carboxylic acids is higher than for $COO\text{-}Ni^{+}$ complexes.[58-60] The presence of -OH functional groups in the biochar could play a role in the higher K_2 values for Ni-ligand complexes than for analogous Zn-ligand complexes.[58-60] It is expected that carboxylic and hydroxyl groups (–OH groups belong both to organic phenols, and to inorganic silanol groups) would be the predominant binding sites of WS, WPC, SSBC 300°C, SSBC 500°C and SSBC 700°C since FTIR, EXAFS and Ni and Zn speciation diagram (Figure S10) revealed that Ni and Zn coordinate at these biochar surface sites.

Using the binding constant (K) values for individual metals (Ni and Zn) determined in biochar-metal adsorption experiments, and the pK_a values and site concentrations determined

from potentiometric titrations, we predicted the adsorption of Ni(II) and Zn(II) to WS when both metals were present in solution (competitive adsorption). This exercise tests the robustness of the SCM approach in predicting metal adsorption to biochar in more complex or environmentally-relevant systems. After making the predictions, we performed the corresponding two-metal adsorption experiments to determine the accuracy of the model predictions (Figure 3A and 3B; S11). In the 17 µM (8.5 µM Ni + 8.5 µM Ni) system, the model slightly over predicts Ni(II) adsorption from pH 4 to 5.5 and under predicts at pH 6.5. Zn(II) adsorption is under predicted across the entire pH range. The two-site model to predict metal adsorption in 170 µM (85 µM Ni + 85 µM Ni) experiments yielded better results. Overall, the predictive models reasonably reproduced experimental results. The observed adsorption of Ni(II) and Zn(II) are quite similar to the 17 µM mixture predictions, but Zn(II) adsorption is higher than is Ni(II) at the 170 µM mixture concentration, showing similar trends as those observed in the single metal experiments (Figure 1).

3.6 Titration calorimetry data analysis

XAS and surface complexation modeling provide information on the coordination environment and the means to quantify surface reactivity, while calorimetric measurements can also provide coordination information and determine the thermodynamic driving force behind the observed reactions. The corrected heats of protonation for to the 3-site protonation model are exothermic for both WS and WPC, with WS being slightly more exothermic (Figure 4A and 4B). The site-specific enthalpies of protonation show that as pH decreases, corrected heats become less exothermic which is a result of a combination of less sites available to protonate and the low pK_a sites being less exothermic (Table 3).[38] The enthalpies of protonation are mildly exothermic to mildly endothermic. Site 1 on both WS and WPC have entropies of protonation of about 80

J/mol K, which are indicative of anionic oxygen ligands that participate in hydrogen bonding with other nearby functional groups. These results indicate the potential for bidentate coordination on the surface, which is consistent with the XAS results. Entropies of protonation > 80 J/mol K like those for sites 2 and 3 for both WS and WPC, are consistent with anionic oxygen ligands that behave more independently without direct interactions with other surface functional groups. The combination of enthalpies, entropies, and log K values are consistent with protonation of monofunctional carboxylic acids, some of which may be close enough together to behave more like multifunctional carboxylic acids. Typical heat flow curves of acid titration and Zn(II) and Ni(II) adsorption titration are presented in SI (Figure S12 and S15).

Corrected heats of Ni and Zn adsorption onto WS and WPC are shown in Figure 4. The stability constants produced from 170 µM Ni and Zn adsorption experiments and the 2-site Ni and Zn adsorption models fit the calorimetric data best for both WS and WPC (Figure 4C to 4F). The enthalpies are mildly endothermic for the L_1Ni^+ complex (<4 kJ/mol) and exothermic for the L_2Ni^+ complex (Table S9). Calorimetric results of Zn adsorption onto both WS and WPC produced mildly exothermic (< -1 kJ/mol) to endothermic enthalpies on surface sites (Figure 4E and 4F and Table S10). Entropies of complexation can provide information on coordination environments based on the disruption or stability of the hydration spheres of ligands and ions.[64-65] Negative entropies of the L_2Ni^+ complex suggests an outer sphere complexation with minimal disruption of hydration spheres and possible complex stabilization through hydrogen bonding. The positive entropies of the L_1Ni^+ complex are consistent with inner sphere complexation, which dehydrates the ligand and metal ion. Positive entropies of Zn complexation indicate dehydration as binding occurs and inner sphere complexation.

Site specific ITC results are dependent on the surface complexation models to derive the enthalpies and entropies of complexation; therefore, consistencies and differences between the ITC and XAS results also have implications for the surface complexation models. Both ITC and XAS indicated the presence of inner sphere surface complexes with anionic oxygen ligands. ITC, which is more sensitive than the XAS measurements, also indicated the presence of some outer sphere complexation. Surface site 2 of WS and WPC produced outer sphere complexes for Ni according to entropies of complexation. The stability constants for these site 2 complexes were also lower than for the site 1 complexes. These two lines of evidence indicate a lower affinity for metal adsorption onto site 2 for WS and WPC. This would result in lower portions of Ni at these sites, which increases the difficulty of detecting these outer sphere complexes with spectroscopic techniques.

Using the thermodynamic parameters derived in this work with the Van't Hoff equation allows us to make predictions about the temperature dependence of proton, Ni, and Zn adsorption onto WS and WPC. These predictions assume that the relative heat capacities of the products and of the reactants (ΔC_P) are zero for the reaction. The magnitude of the enthalpies of protonation are not large enough to impart much temperature dependence on the protonation of the biochar surface. The maximum change in the log K value for protonation of the biochar surface from 25°C is approximately 0.2 over the temperature range of 5 to 75°C. The temperature dependence of metal adsorption is predicted to be more substantial given that the enthalpies of Ni and Zn adsorption onto site 2 are approximately an order of magnitude more endothermic or exothermic than protonation enthalpies. For example, the change in log K for Ni adsorption onto WPC site 2 is predicted to increase by approximately 2 at 75°C. The log K for Zn adsorption onto WS site 2 is predicted increase by approximately 2.5 at 75°C. These

predictions illustrate the utility of calorimetric investigations and the potential temperature dependence of Ni and Zn adsorption onto the biochar investigated.

4. ENVIRONMENTAL IMPLICATIONS

Biochar is a promising material for the adsorptive removal of metals and organics from water. This is the first study combining spectroscopic data (EXAFS and FTIR) with thermodynamic data (SCM and ITC) to explore molecular scale metal adsorption at biochar surface functional groups. The study demonstrates that feedstock type and pyrolysis temperature during biochar production profoundly influence biochar characteristics, including chemical properties, structure, and metal binding mechanisms. Higher reactive site densities/functional group concentrations for metal removal are obtained from biochar produced at lower pyrolysis temperature (~300°C), and Ni(II) and Zn(II) adsorption densities are directly related to the reactive site densities and molar O/C ratios of biochar. Thus, to improve the performance of metal removal and soil amendment, biochar selection should be made on a case-by-case based on the biochar physical and chemical properties.

EXAFS characterization combined with FTIR analysis further suggest that Ni(II) and Zn(II) sorption to biochar primarily occurred through the coordination of carboxyl anions (-COOH) and hydroxyl (-OH) with Ni(II) and Zn(II). The SCM approach applied in this study accurately predicts the metal adsorption behavior to the surface of the biochar for single (Ni or Zn) and multi-metal (Ni + Zn) systems. By using a combined SCM-ITC approach, the thermodynamic parameters of the metal-biochar surface complexation reactions were determined. Enthalpies of Ni- and Zn-ligand reactions were consistent with the presence of anionic oxygen ligand corresponding to –COOH and –OH functional groups. The development of predictive SCMs is a key step towards optimized design and operation of biochar-based water treatment systems, which have promise to replace more costly technologies such as activated

carbon. These combined approaches will help to identify the reaction pathways of metals with biochar, and provide new tools to remove metals from water using biochar in variable water chemistries.

ASSOCIATED CONTENT

Supporting Information

Includes a detailed discussion for materials, biochar characterization, potentiometric titrations, adsorption and ITC data modeling. Ni and Zn aqueous speciation diagram (Figure S1), Ni and Zn adsorption kinetics (Figure S2), XRD pattern (Figure S3), SEM images (Figure S4), EDS spectra (Figure S5), potentiometric titration (Figure S6), FT-IR spectra (Figure S7), surface area normalized adsorption densities of Ni and Zn (Figure S8), 1-site adsorption model of Ni and Zn (Figure S9), 1-site competitive adsorption model (Figure S10), Ni and Zn speciation distribution after adsorption (Figure S11), heat flow curve for acid titration (Figure S12), heat flow curves of WS titrations with Ni(II) and Zn(II) (Figure S13), heat flow curves of WPC titrations with Ni(II) and Zn(II) (Figure S14), heat flow curves of background heats for Ni(II) and Zn(II) (Figure S15), percent moisture contents, mobile matter, ash content and fixed matter (Table S1), pH, elemental composition, molar ratio, BET surface area, and pore volume (Table S2), elemental composition estimated from SEM-EDS analysis (Table S3), leaching data (Table S4), EXAFS fit results for Ni adsorption (Table S5), EXAFS fit results for Zn adsorption (Table S6), aqueous Ni (II) and Zn (II) hydrolysis reactions (Table S7), stability constant obtained from 1-site best-fit models (Table S8), site-specific thermodynamic parameters for the adsorption of Ni (Table S9), and site-specific thermodynamic parameters for the adsorption of Zn (Table S10).

AUTHOR INFORMATION

Corresponding Author

*Phone: +1-780-492-8019; Fax: 780-492-2030; email: alessi@ualberta.ca.

ACKNOWLEDGEMENTS

This work was supported by NSERC Discovery Grants to D.S.A. and K.O.K. XAS analyses were performed at the Hard X-ray MicroAnalysis (HXMA) beamline in the Canadian Light Sources (CLS). The CLS is funded by the Canadian Foundation of Innovation (CFI), the National Science and Engineering Research Council (NSERC), The National Research Council (NRC), the Canadian Institutes of Health Research (CIHR), the Government of Saskatchewan, and the University of Saskatchewan. We appreciate three anonymous reviewers whose comments and suggestions helped us to improve the manuscript.

REFERENCES

1. Ahmad, M., Rajapaksha, A.U., Lim, J.E., Zhang, M., Bolan, N., Mohan, D., Vithanage, M., Lee, S.S. and Ok, Y.S. Biochar as a sorbent for contaminant management in soil and water: a review. *Chemosphere*. 2014, 99: 19-33.
2. Cao, X.D., Ma, L.N., Gao, B., Harris, W. Dairy-manure derived biochar effectively sorbs lead and atrazine. *Environ. Sci. Technol.* 2009, 43, 3285-3291.
3. Cao, X., Harris,W. Properties of dairy-manure-derived biochar pertinent to its potential use in remediation. *Bioresour. Technol.* 2010, 101, 5222-5228.
4. Alam, M. S., Cossio, M., Robinson, L., Kenney, J. P. L., Wang, X., Konhauser, K. O., MacKenzie, M. D., Ok, Y. S., Alessi, D. S. Removal of organic acids from water using biochar and petroleum coke. *Environ. Technol. & Innova.* 2016, 6: 141-151.
5. Choppala, G., Bolan, N., Megharaj, M., Chen, Z. and Naidu, R. The influence of biochar and black carbon on reduction and bioavailability of chromate in soils. *J. Environ. Quali.* 2012, 41(4): 1175-1184.
6. Mohan, D. and Pittman, C.U. Activated carbons and low cost adsorbents for remediation of tri-and hexavalent chromium from water. *J. Hazard. Mater.* 2006, 137(2): 762-811.
7. Mohan, D., Rajput, S., Singh, V.K., Steele, P.H. and Pittman, C.U. Modeling and evaluation of chromium remediation from water using low cost bio-char, a green adsorbent. *J. Hazard. Mater*. 2011, 188(1): 319-333.
8. Thompson, K.A., Shimabuku, K.K., Kearns, J.,P, Knappe, D.R.U., Summer, S., and Cook, S.M. Environmental Comparison of Biochar and Activated Carbon for Tertiary Wastewater Treatment. *Environ. Sci. Technol.* 2016, 50, 11253-11262.
9. Yang, F., Zhao, L., Gao, B., Xu, X.Y., Cao, X.D. The interfacial behavior between biochar and soil minerals and its effect on biochar stability. *Environ. Sci. Technol.* 2016, 50, 2264e2271.
10. Woolf, D., Amonette, J. E., Street-Peroott, F. A., Lehmann, J., Joseph, S. Sustainable biochar to mitigate global climate change. *Nat. Commun.* 2010, 1, 1-9.
11. Zhou, B., Wang, Z., Shen, D., Shen, F., Wu, C. and Xiao, R. Low cost earthworm manure-derived carbon material for the adsorption of Cu^{2+} from aqueous solution: Impact of pyrolysis temperature. *Ecologi. Eng.* 2017, 98: 189-195.
12. Ahmad, M., Lee, S.S., Dou, X., Mohan, D., Sung, J.K., Yang, J.E., Ok, Y.S. Effects of pyrolysis temperature on soybean stover- and peanut shell-derived biochar properties and TCE adsorption in water. *Bioresour. Technol.* 2012, 118, 536-544.
13. Chen, Z., Chen, B., Chiou, C.T. Fast and slow rates of naphthalene sorption to biochars produced at different temperatures. *Environ. Sci. Technol.* 2012, 46, 11104-11111.
14. Scheidegger, A. M.; Lamble, G. M.; Sparks, D. L. Investigations of Ni sorption on pyrophyllite: An XAFS study. *Environ. Sci. Technol.* 1996, 30, 548−554.
15. He, Z. L.; Yang, X. E.; Stoffella, P. J. Trace elements in agroecosystems and impacts on the environment. *J. Trace Elem. Med. Biol.* 2005, 19 (2−3), 125−140.
16. Koretsky, C. The significance of surface complexation reactions in hydrologic systems: a geochemist's perspective. *J. Hydrology.* 2000, 230(3): 127-171.
17. Bethke, C.M., Brady, P.V. How the K-d approach undermines groundwater cleanup. *Ground Water*. 2000, 3, 435-443.

18. Borrok, D., Turner, B.F. and Fein, J.B. A universal surface complexation framework for modeling proton binding onto bacterial surfaces in geologic settings. *Ameri. J. Sci.* 2005, 305(6-8): 826-853.
19. Alessi, D.S. and Fein, J.B. Cadmium adsorption to mixtures of soil components: Testing the component additivity approach. *Chem. Geo.* 2010, 270(1): 186-195.
20. Beveridge, T. and Murray, R. Sites of metal deposition in the cell wall of *Bacillus subtilis*. *J. Bacteriology.* 1980, 141(2): 876-887.
21. Flynn, S.L., Szymanowski, J.E.S., Fein, J.B. Modeling bacterial metal toxicity using a surface complexation approach. *Chem. Geol.* 2014, 374, 110-116.
22. Manning, B.A. and Goldberg, S. Adsorption and stability of arsenic (III) at the clay mineral-water interface. *Environ. Sci. Technol*. 1997, 31(7): 2005-2011.
23. Marmier, N., Delisée, A. and Fromage, F. Surface complexation modeling of Yb (III) and Cs (I) sorption on silica. *J. Colloid Interface Sci.* 1999, 212(2): 228-233.
24. B. Hu, Q. Hu, D. Xu, C. Chen, The adsorption of U(VI) on carbonaceous nanofibers: A combined batch, EXAFS and modeling techniques, *Sep. Purif. Technol.* 2017, 175: 140-146.
25. Lalonde, S., Konhauser, K. O., Amskold, L., McDermott, T., Inskeep, B. P. Chemical reactivity of microbe and mineral surfaces in hydrous ferric oxide depositing hydrothermal springs. *Geobiology*. 2007a, 5: 219-234.
26. Liu, Y., Alessi, D. S., Owttrim, G. W., Petrash, D. A., Mloszewska, A. M., Lalonde, S. V., Martinez, R. E., Zhou, Q., Konhauser, K. O. Cell surface reactivity of Synechococcus sp. PCC 7002: Implications for metal sorption from seawater. *Geochim. Cosmochim. Acta* 2015, 169: 30-44.
27. Dong, X., Ma, L.Q., Zhu, Y., Li, Y., Gu, B. Mechanistic investigation of mercury sorption by Brazilian pepper biochars of different pyrolytic temperatures based on X-ray photoelectron spectroscopy and flow calorimetry. *Environ. Sci. Technol.* 2013, 47, 12156-12164.
28. Zhang, Y., Luo, W. Adsorptive removal of heavy metal from acidic wastewater with biochar produced from anaerobically digested residues: Kinetics and surface complexation modeling. *BioResources* 2014, 9(2): 2484-2499.
29. Vithanage, M., Rajapaksha, A.U., Ahmad, M., Uchimiya, M., Dou, X., Alessi, D.S. and Ok, Y.S. Mechanisms of antimony adsorption onto soybean stover-derived biochar in aqueous solutions. *J. Environ. Manage.* 2015, 151: 443-449.
30. Alam, M.S., Swaren, L, Gunten, K.V., Cossio, M., Robbins, L.J., Flynn, S.L., Konhauser, K.O, Alessi, D. S. Application of surface complexation modeling to trace metals uptake by biochar-amended agricultural soils. *App. Geochem.* 2018, 88:103-112.
31. Tan, X., Hu, J., Montavon, G. and Wang, X. Sorption speciation of nickel (II) onto Ca-montmorillonite: Batch, EXAFS techniques and modeling. *Dalton Trans.* 2011, 40(41): 10953-10960.
32. Betts, A.R., Chen, N., Hamilton, J.G., Peak, D. Rates and mechanisms of Zn^{2+} adsorption on a meat and bonemeal biochar. *Environ. Sci. Technol.* 2013, 47, 14350-14357.
33. Scheidegger, A. M., Lamble, G. M., Sparks, D. L. Spectroscopic evidence for the formation of mixed-cation hydroxide phases upon metal sorption on clays and aluminum oxides. *J. Colloid Interface Sci.* 1997, 186, 118-128.
34. Elzinga, E. J., Reeder, R. J. X-ray absorption spectroscopy study of Cu(II) and Zn(II) adsorption complexes at the calcite surface: Implications for site-specific metal

598 incorporation preferences during calcite crystal growth. *Geochim. Cosmochim. Acta*
599 2002, 66, 3943-3954.
600 35. Drew Gorman-Lewis. Enthalpies and Entropies of Cd and Zn Adsorption onto Bacillus
601 licheniformis and Enthalpies and Entropies of Zn Adsorption onto Bacillus subtilis from
602 Isothermal Titration Calorimetry and Surface Complexation Modeling. *Geobio. J.* 2014,
603 31: 383-359.
604 36. Zoe¨ R. Harrold and Drew Gorman-Lewis. Thermodynamic analysis of *Bacillus subtilis*
605 endospore protonation using isothermal titration calorimetry. *Geochim. Cosmochim. Acta*
606 2013, 109: 296-305.
607 37. Gorman-Lewis D. Enthalpies of proton adsorption onto *Bacillus licheniformis* at 25, 37,
608 50, and 75◦C. *Geochim Cosmochim Acta* 2011, 75:1297-1307.
609 38. Gorman-Lewis D., Fein J.B., Jensen M.P. Enthalpies and entropies of proton and
610 cadmium adsorption onto Bacillus subtilis bacterial cells from calorimetric
611 measurements. *Geochim Cosmochim Acta* 2006, 70:4862-4873.
612 39. Chen, Z., Chen, B., Zhou, D., Chen, W. Bisolute Sorption and Thermodynamic Behavior
613 of Organic Pollutants to Biomass-derived Biochars at Two Pyrolytic Temperatures.
614 *Environ. Sci. Technol.* 2012, 46, 12476-12483.
615 40. Ravel B. and Newville M. ATHENA, ARTEMIS, HEPHAESTUS: data analysis for X-
616 ray absorption spectroscopy using IFEFFIT. *J. Synchrotron Rad.* 2005, **12**, pp 537-541.
617 41. Ressler T. WinXAS: A new software package not only for the analysis of energy-
618 dispersive XAS data. *J. de Physique IV*. 1997, **7**(C2): 269-270.
619 42. Ankudinov, A., Rehr, J.J. Theory of solid state contributions to the x-ray elastic
620 scattering amplitude. *Phys. Rev. B.* 2000, 62, 2437-2445.
621 43. Rihs, S. Gaillard, C., Reich, T., Kohler, S. Uranyl sorption onto brinssite: A surface
622 complexation modeling and EXAFS study. *Chem. Geo.* 2014. 373, 59-70.
623 44. Grenthe, I., Ots, H., Ginstrup, O. A calorimetric determination of the enthalpy of
624 ionization of water and the enthalpy of protonation of THAM at 5, 20, 25, 35, and 50C.
625 *Acta Chemica Scandinavica.* 1970, 24:1067-1080.
626 45. Keiluweit, M., Nico, P. S., Johnson, M. G., Kleber, M. Dynamic molecular structure of
627 plant biomass-derived black carbon (biochar). *Environ. Sci. Technol.* 2010, 44, 1247-
628 1253.
629 46. Chen, Z., Xiao, X., Chen, B., Zhu, L. Quantification of chemical states, dissociation
630 constants and contents of oxygen-containing groups on the surface of biochars produced
631 at different temperatures. *Environ. Sci. Technol.* 2015, 49 (1), 309-317.
632 47. Spokas, K.A. Review of the stability of biochar in soils: predictability of O: C molar
633 ratios. *Carbon Manage.* 2010, 1(2): 289-303.
634 48. Liu, Y., Yang, M., Wu, Y.Wang, H., Chen, Y., Wu, W. Reducing CH_4 and CO_2
635 emissions from waterlogged paddy soil with biochar. *J. Soils Sediments.* 2011, 11: 930-
636 939.
637 49. Herbelin, A. and Westall, J. FITEQL-a computer program for determination of chemical
638 equilibrium constants from experimental data version 3.2 user's manual. Department of
639 Chemistry, Oregon State University, Corvallis, OR, Report.: 1996, 96-01.
640 50. Chia, C. H., Gong, B., Joseph, S. D., Marjo, C. E., Munroe, P., Rich, A. M. Imaging of
641 mineral-enriched biochar by FTIR, Raman and SEM−EDX. *Vib. Spectrosc.* 2012, 62,
642 248-257.

51. Chen, B., Zhou, D., Zhu, L. Transitional adsorption and partition of nonpolar and polar aromatic contaminants by biochars of pine needles with different pyrolytic temperatures. *Environ. Sci. Technol.* 2008**,** 42(14), 5137-5143.
52. Li, M., Liu, Q., Lou, Z., Wang, Y. Method to Characterize Acid-Base Behavior of Biochar: Site Modeling and Theoretical Simulation. *ACS Sustainable Chem. Eng.* 2014, 2 (11), 2501-2509.
53. Achadu, O.J., Ayejuyo, O.O., Ako, F.E., Dalla, C.L. and Olaoye, O.O. Synchronous Adsorption of Cadmium and Lead ions from Aqueous Media by Rice Husk Ash and Sodium Dodecyl Sulfate Combination. *Int. J. of Modern Analytical and Separation Sci.*, 2014, 3(1), 20-39.
54. Guo, Y., Bustin, R. M. FTIR spectroscopy and reflectance of modern charcoals and fungal decayed woods: implications for studies of inertinite in coals. *Int. J. Coal Geol.* 1998**,** 37(1-2), 29-53.
55. Pastorova, I., Botto, R. E., Arisz, P., Boon, J. Cellulose char structure - a combined analytical PY-GC-MS, FTIR, and NMR-study. *Carbohydr. Res.* 1994**,** 262(1), 27-47.
56. Xiao, X. and Chen, B. A Direct Observation of the Fine Aromatic Clusters and Molecular Structures of Biochars. *Environ. Sci. Technol.* 2017, 51, 5473-5482.
57. Shahata, M.M. Adsorption of some heavy metal ions by used different immobilized substances on silica gel. *Arabian J. of Chem.* 2016, 9(6), 755-763.
58. Yasuda, M., Yamaskik, K., and Ohtaki, H. Stability of complexes of several carboxylic acids formed with bivalent metals. *Bull. Chem. Sot. Japan.* 1960, 33, 1067-1070
59. Xia K., Bleam W., and Helmke P. A. Studies of the nature of binding sites of first row transition elements bound to aquatic and soil humic substances using X-ray absorption spectroscopy. *Geochim. Cosmochim. Act*. 1997a, 61, 2223-2235.
60. Ma, Q. Y., Traina, S. J, Logan, T. J., Ryan, J. A. Effects of aqueous Al, Cd, Cu, Fe(II), Ni, and Zn on Pb immobilization by hydroxyapatite. *Environ. Sci. Technol.* 1994, 28, 1219-1228.
61. Fein, J.B., Daughney, C.J., Yee, N., Davis, T.A. A chemical equilibriummodel formetal adsorption onto bacterial surfaces. *Geochim. Cosmochim. Acta*. 1997, 61, 3319–3328.
62. Fein, J.B., Boily, J. F., Yee, N., Gorman-Lewis, D., Turner, B.F. Potentiometric titrations of Bacillus subtilis cells to low pH and a comparison of modeling approaches. *Geochim. Cosmochim. Acta. 2005,* 69, 1123-1132.
63. Fowle, D.A., Fein, J.B. Competitive adsorption of metal cátions onto two gram positive bacteria: testing the chemical equilibrium model. *Geochim. Cosmochim. Acta. 1999,* 63, 3059-3067.
64. Choppin, G.R. Factors in Ln(III) complexation. J. Alloy. Compd. 1997, 249 (1–2), 1–8.
65. Jensen, M.P., Morss, L.R., Beitz, J.V., Ensor, D.D. Aqueous complexation of trivalent lanthanide and actinide cations by N,N,N0,N0-Tetrakis (2-pyridylmethyl) ethylenediamine. *J. Alloy. Compd.* 2000, 303/304, 137-141.

Figure 1. Adsorption of Ni and Zn onto WS, WPC, SSBC 300°C, SSBC 500°C and SSBC 700°C, showing the 2-site best-fit adsorption models: A. 17µM Ni; B. 170µM Ni; C. 17 µM Zn; D. 170µM Zn. The open symbols represent experimental data and solid lines represent best-fit models.

Figure 2. EXAFS signals weighted by k^3 spectra and R space curve fitting results for Ni and Zn adsorbed to WS. A. k^3 spectra of Ni; B. R space of Ni; C. k^3 spectra of Zn; D. R space of Zn; (1) 170µM Ni; (2) 85µM Ni; (3) 17µM Ni; (4) 170µM Zn; (5) 85µM Ni and (6) 17µM Zn.

Figure 3. Competitive adsorption of Ni and Zn (A and B) onto WS A. 8.5µM Ni + 8.5 µM Zn with the 2-site predictive adsorption model; B. 85µM Ni + 85 µM Zn with 2-site predictive adsorption model. The open symbols represent experimental data, and solid lines and dashed lines represent predictive models.

Figure 4. Corrected heat generated from proton, and Ni and Zn adsorption titrations of WS and WPC. A. Proton adsorption on WS; B. Proton adsorption on WPC; C. Ni adsorption on WS; D. Zn adsorption on WS; E. Ni adsorption on WPC; F. Zn adsorption on WPC. The open symbols and solid lines represent the experimental data and the fit, respectively. The open symbols and solid lines in blue and green colors in proton adsorption model (A,B) represents replicates. The Ni and Zn adsorption titration experimental data (open symbol) also have replicates.

Table 1. Parameters obtained from 3-sit best-fit protonation models of potentiometric titration data of WS, WPC, SSBC 300°C, SSBC 500°C and SSBC 700°C.

Table 2. Stability constants obtained from 2-site adsorption model best-fits of Ni and Zn adsorption to WS, WPC, SSBC 300°C, SSBC 500°C and SSBC 700°C.

Table 3. Site-specific thermodynamic parameters for the reaction of H^+ with biochar, derived from calorimetric titrations and the 3-site model calculated from potentiometric titration data.

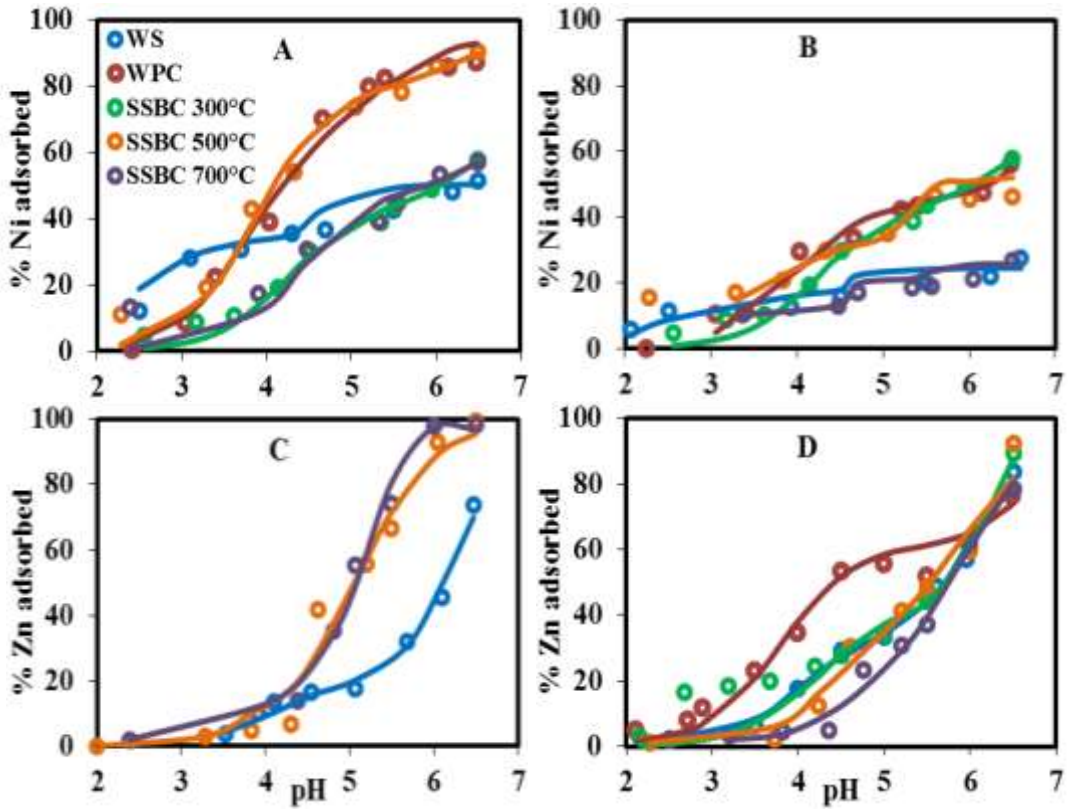

Figure 1. Adsorption of Ni and Zn onto WS, WPC, SSBC 300°C, SSBC 500°C and SSBC 700°C, showing the 2-site best-fit adsorption models: A. 17µM Ni; B. 170µM Ni; C. 17 µM Zn; D. 170µM Zn. The open symbols represent experimental data and solid lines represent best-fit models.

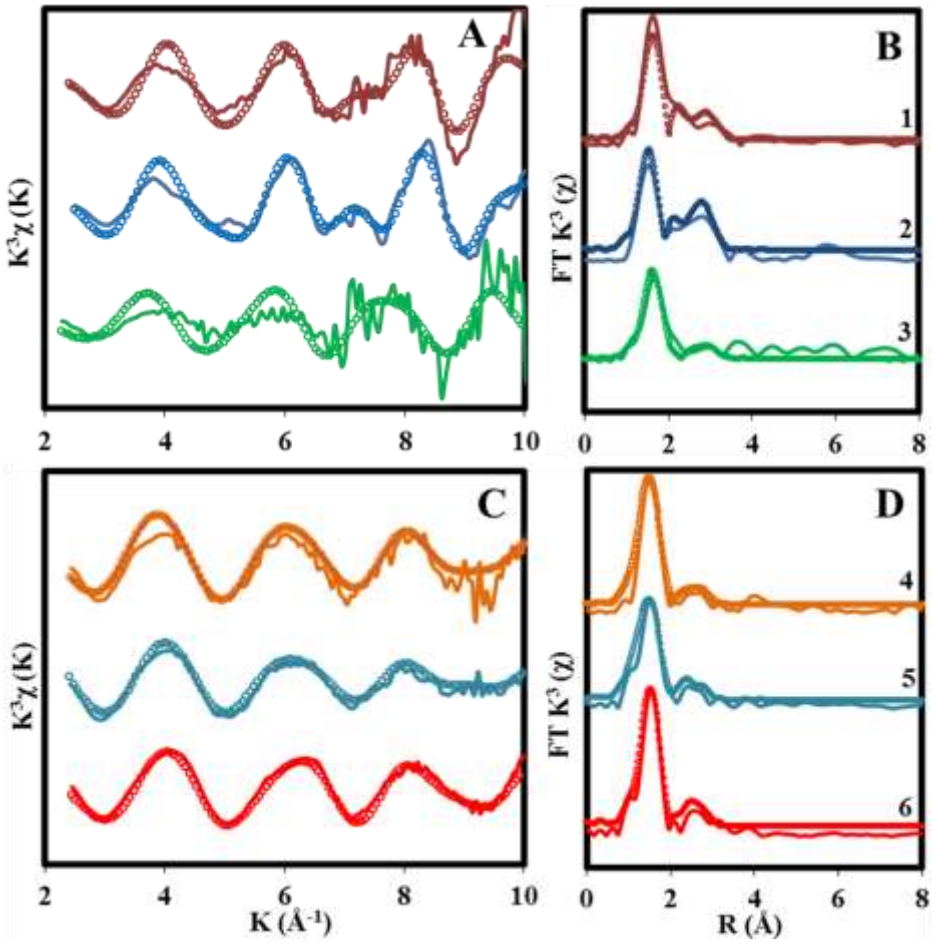

748

749 Figure 2. EXAFS signals weighted by k^3 spectra and R space curve fitting results for Ni and Zn
750 adsorbed to WS. A. k^3 spectra of Ni; B. R space of Ni; C. k^3 spectra of Zn; D. R space of Zn; (1)
751 170μM Ni; (2) 85μM Ni; (3) 17μM Ni; (4) 170μM Zn; (5) 85μM Ni and (6) 17μM Zn.

752

753

754

755

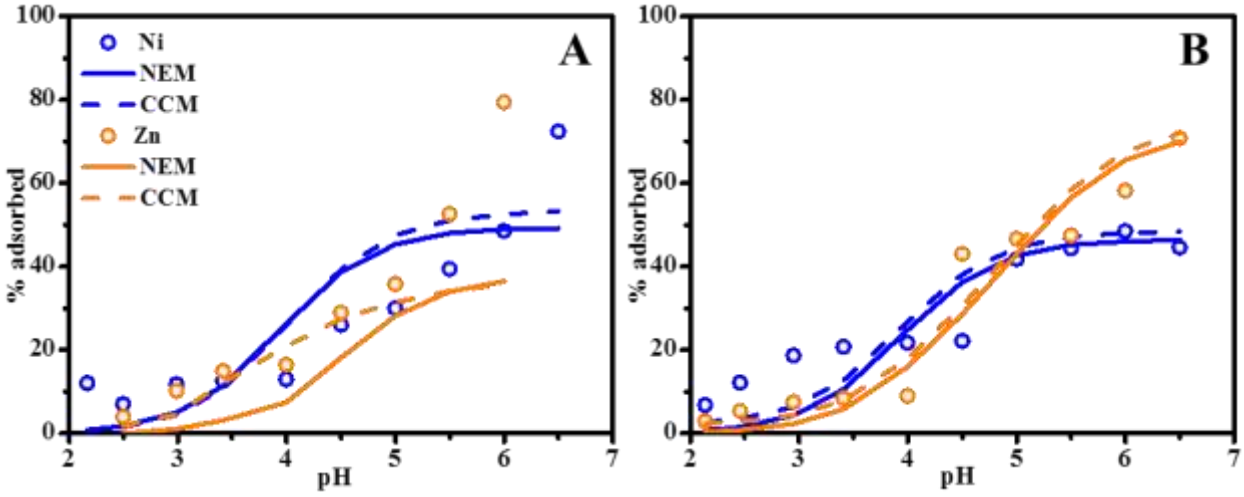

Figure 3. Competitive adsorption of Ni and Zn (A and B) onto WS A. 8.5µM Ni + 8.5 µM Zn with the 2-site predictive adsorption model; B. 85µM Ni + 85 µM Zn with 2-site predictive adsorption model. The open symbols represent experimental data, and solid lines and dashed lines represent predictive models.

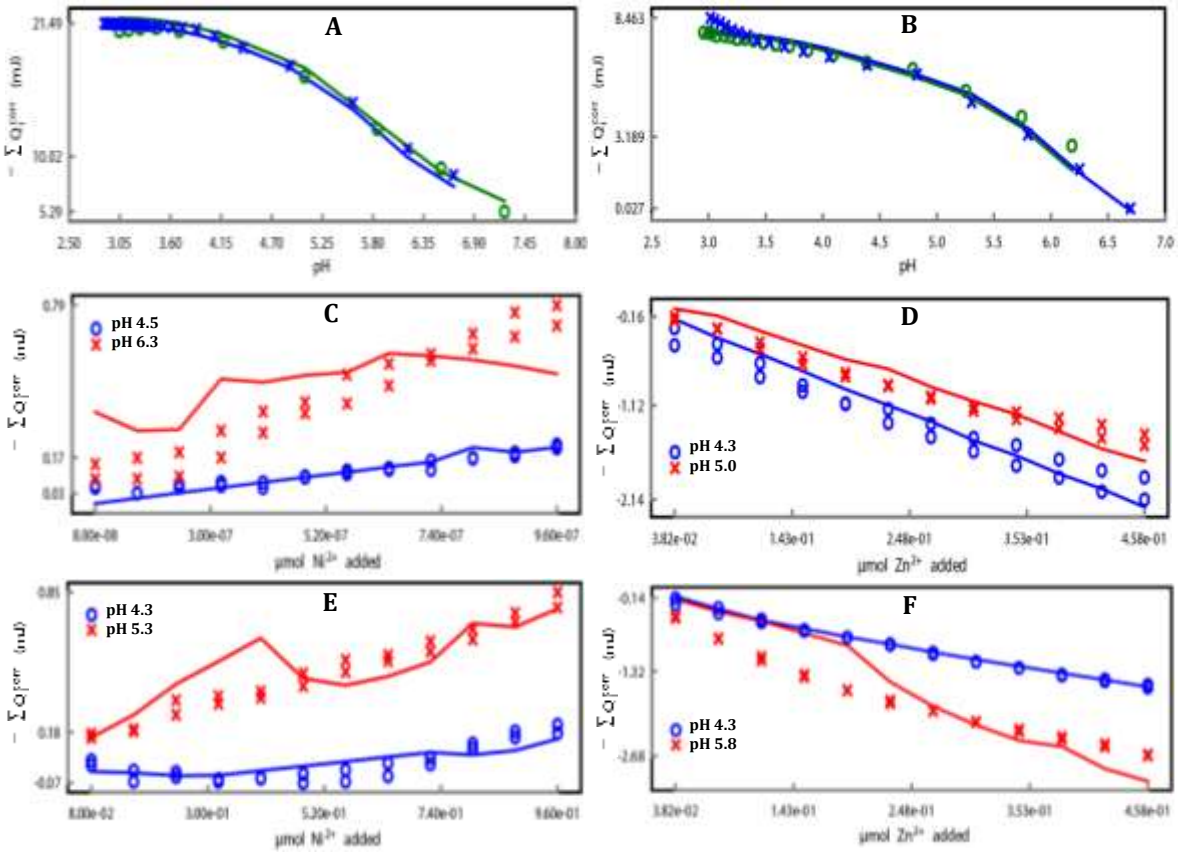

Figure 4. Corrected heat generated from proton, and Ni and Zn adsorption titrations of WS and WPC. A. Proton adsorption on WS; B. Proton adsorption on WPC; C. Ni adsorption on WS; D. Zn adsorption on WS; E. Ni adsorption on WPC; F. Zn adsorption on WPC. The open symbols and solid lines represent the experimental data and the fit, respectively. The open symbols and solid lines in blue and green colors in proton adsorption model (A,B) represents replicates. The Ni and Zn adsorption titration experimental data (open symbol) also have replicates.

Table 1. Parameters obtained from 3-site best-fit protonation models, of titration data of WS, WPC, SSBC 300°C, SSBC 500°C and SSBC 700°C.

Biochar	Total Sites	pKa_1	pKa_2	pKa_3	Site1 concentration (mol/g)	Site2 concentration (mol/g)	Site3 concentration (mol/g)	Total reactive site (mol/g)	Surface area Reactive site densities (mol/m^2)	V(Y)
WS	3	4.24	5.82	7.87	7.5E-04	1.2E-04	1.0E-04	9.7E-04	3.7E-05	5.71
WPC	3	4.23	6.18	7.94	9.8E-04	1.1E-04	1.4E-04	1.2E-03	5.4E-06	11.43
SSBC 300°C	3	4.50	7.00	8.42	1.1E-03	3.3E-04	4.1E-04	1.8E-03	4.0E-04	1.55
SSBC 500°C	3	4.54	7.21	8.55	2.7E-03	2.9E-04	1.0E-03	4.0E-03	1.5E-04	2.44
SSBC 700°C	3	4.70	7.76	9.30	8.0E-04	5.7E-04	6.8E-04	2.0E-03	3.6E-05	1.33

Table 2. Stability constants obtained from 2-site best-fit adsorption models of Ni and Zn adsorption to WS, WPC, SSBC 300°C, SSBC 500°C and SSBC 700°C.

Biochar	Ni 17 µM		V(Y)	Ni 170 µM		V(Y)	Zn 17 µM		V(Y)	Zn 170 µM		V(Y)
	log K_1^*	log $K_2^\dagger$		log K_1^*	log $K_2^\dagger$		log K_1^*	log $K_2^\dagger$		log K_1^*	log $K_2^\dagger$	
WS	2.74	0.40	3.7	2.24	2.22	14	2.17	2.42	0.2	2.44	2.82	5
WPC	2.83	4.68	0.4	2.53	1.88	23	NA	NA	NA	2.83	2.38	20
SSBC 300°C	2.50	3.5	0.2	1.90	2.90	12	NA	NA	NA	2.45	3.0	9
SSBC 500°C	2.74	4.61	0.5	2.24	2.61	20	1.34	5.21	2	1.84	4.61	36
SSBC 700°C	2.70	3.76	1	2.20	2.76	13	2.50	5.16	0.9	2.20	4.76	24

NA = Not available

$^*R\text{-}A_1^- + M^{++} \leftrightarrow R\text{-}A_1(M)^+$

$^\dagger R\text{-}A_2^- + M^{++} \leftrightarrow R\text{-}A_2(M)^+$

Table 3. Site-specific thermodynamic parameters for the reaction of H^+ derived from calorimetric titrations, and 3-site models from potentiometric titration data.

Protonated Sites	logK	Gibbs free energy, $\Delta G_r°$ (KJ/mol)	Enthalpy, $\Delta H_r°$ (KJ/mol)	$-T\Delta S_r°$ (KJ/mol)	Entropy, $\Delta S_r°$ (J/molK)
			WS		
HL1	4.24(0.05)	-24.20(0.29)	-0.18(0.02)	-24.02(0.29)	80 (1)
HL2	5.82(0.17)	-33.22(0.97)	-3.88(0.20)	-29.34(0.99)	98 (3)
HL3	7.87(0.09)	-44.92(0.51)	-2.93(0.15)	-41.99(0.53)	141 (2)
			WPC		
HL1	4.23(0.02)	-24.15(0.11)	-0.09(0.01)	-24.06(0.11)	81(1)
HL2	6.18(0.15)	-35.28(0.86)	-2.97(0.10)	-32.31(0.86)	108 (3)
HL3	7.94(0.07)	-45.32(0.40)	1.54(0.12)	-46.86(0.42)	157 (1)

TOC